

RL-TR-96-27
Final Technical Report
March 1996



SILICA-BASED OPTICAL TIME-SHIFT NETWORK

Hughes Research Laboratories

W. Ng, R. Loo, S. Livingston, and J.J. Lee

APPROVED FOR PUBLIC RELEASE; DISTRIBUTION UNLIMITED.

19960626 018

Rome Laboratory
Air Force Materiel Command
Rome, New York

DTIC QUALITY INSPECTED 1

This report has been reviewed by the Rome Laboratory Public Affairs Office (PA) and is releasable to the National Technical Information Service (NTIS). At NTIS, it will be releasable to the general public, including foreign nations.

RL-TR-96-27 has been reviewed and is approved for publication.

APPROVED:

James R. Hunter

JAMES R. HUNTER
Project Engineer

FOR THE COMMANDER:

Gary D. Barmore
GARY D. BARMORE, Major, USAF
Deputy Director of Surveillance & Photonics

If your address has changed or if you wish to be removed from the Rome Laboratory mailing list, or if the addressee is no longer employed by your organization, please notify Rome Laboratory (OCPC), Rome NY 13441. This will assist us in maintaining a current mailing list.

Do not return copies of this report unless contractual obligations or notices on a specific document require that it be returned.

REPORT DOCUMENTATION PAGE

Form Approved
OMB No. 0704-0188

Public reporting burden for this collection of information is estimated to average 1 hour per response, including the time for reviewing instructions, searching existing data sources, gathering and maintaining the data needed, and completing and reviewing the collection of information. Send comments regarding this burden estimate or any other aspect of this collection of information, including suggestions for reducing this burden, to Washington Headquarters Services, Directorate for Information Operations and Reports, 1215 Jefferson Davis Highway, Suite 1204, Arlington, VA 22202-4302, and to the Office of Management and Budget, Paperwork Reduction Project (0704-0188), Washington, DC 20503.

1. AGENCY USE ONLY (Leave Blank)		2. REPORT DATE March 1996	3. REPORT TYPE AND DATES COVERED Final Aug 93 - Aug 95
4. TITLE AND SUBTITLE SILICA-BASED OPTICAL TIME-SHIFT NETWORK		5. FUNDING NUMBERS C - F30602-93-C-0092 PE - 63726F PR - 2863 TA - 92 WU - 66	
6. AUTHOR(S) W. Ng, R. Loo, S. Livingston, and J. J. Lee		8. PERFORMING ORGANIZATION REPORT NUMBER N/A	
7. PERFORMING ORGANIZATION NAME(S) AND ADDRESS(ES) Hughes Research Laboratories 3011 Malibu Canyon Road Malibu CA 90265		10. SPONSORING/MONITORING AGENCY REPORT NUMBER RL-TR-96-27	
9. SPONSORING/MONITORING AGENCY NAME(S) AND ADDRESS(ES) Rome Laboratory/OCPC 25 Electronic Pky Rome NY 13441-4515		11. SUPPLEMENTARY NOTES Rome Laboratory Project Engineer: James R. Hunter/OCPC/(315) 330-7045	
12a. DISTRIBUTION/AVAILABILITY STATEMENT Approved for public release; distribution unlimited.		12b. DISTRIBUTION CODE	
13. ABSTRACT (Maximum 200 words) The objective of this program was to design, fabricate, package, and demonstrate a silica-waveguide time-delay network for evaluation in a phased array antenna testbed. Specifically, a 4-bit silica-waveguide time-shifter module, with programmable time-delay steps of 0.248 nsec has been successfully developed. The silica-waveguide module was inserted into a 96 element L-band array, controlling the central column. Extensive demonstration and evaluation verified that the antenna has better than 50% instantaneous bandwidth scanning angles \pm 60 degrees. In addition, an improved, smaller package was developed and evaluated, resulting in a "folded-chip" package with dimensions of approximately 13 cm x 7 cm.			
14. SUBJECT TERMS Optical waveguide, Silica waveguide, Optical true time delay, Photonic true time delay		15. NUMBER OF PAGES 44	16. PRICE CODE
17. SECURITY CLASSIFICATION OF REPORT UNCLASSIFIED	18. SECURITY CLASSIFICATION OF THIS PAGE UNCLASSIFIED	19. SECURITY CLASSIFICATION OF ABSTRACT UNCLASSIFIED	20. LIMITATION OF ABSTRACT UL

CONTENTS

	Page
1 EXECUTIVE SUMMARY	1
2 INTRODUCTION	2
3 DESIGN OF 4-BIT OPTOELECTRONIC-SWITCHED SILICA-WAVEGUIDE TIME-SHIFTER	8
3.1 Bending Losses of Curved Integrated Optical Waveguides	9
3.2 Design of 4-Bit Optoelectronic-Switched Time-Delay Network	11
3.3 Delay-Line Design For The 4-Bit Silica-Waveguide Time-Delay Network	13
4 CHARACTERIZATION OF THE SILICA-WAVEGUIDE OPTICAL TIME-SHIFT NETWORK	17
4.1 Measurements of the Optical Insertion Loss.....	17
4.2 Measurements of the Differential RF Insertion Phase	19
4.3 Measurements of the Synthesized Pulse Response	20
5 INSERTION OF SILICA-WAVEGUIDE MODULE INTO L-BAND ARRAY AND SUMMARY	25
5.1 Insertion of Silica-Waveguide Module into L-Band Conformal Array	25
5.2 Folded-Chip Version of the Silica-Waveguide Module	26
5.3 Conclusion	29
6 REFERENCES.....	31

ILLUSTRATIONS

	Page
1 SEM Micrograph of Buried Silica-waveguide.....	3
2 SEM Micrograph of GaAs/GaAlAs Rib Waveguide	4
3 Fabrication Sequence of Buried Silica Waveguides by Flame Hydrolysis (FHD)	4
4 (a) Outer Dimensions of the ARPA/Rome L-band Conformal Array; 4(b) The Antenna Aperture and Beam-forming Network of the Array	6
5 Radiation Loss from an Optical Mode Guided Around a Waveguide Bend	12
6 Transition Loss Occuring at a Junction Joining a Straight and a Curved Waveguide Segment.....	12
7 Schematic of 4-bit Silica-waveguide Optical Time-shift Network.....	12
8 Waveguide Layout of Chip I.....	14
9 Waveguide "Loop" of Chip I	15
10 Waveguide Layout of Chip II	16
11 (a) Photograph of Silica Waveguide Chips I and II Butt-coupled Against 4 \times 4 Star-coupler; (b) Photograph of Al-housing and Fiber-pigtails for the Waveguide Chips	18
12 Relative RF Insertion Phase Vs. Frequency Between the Reference Line $L_0=L_1+L_5$ and the Delay-line Paths for (i) $L=L_0+\Delta L$, and (ii) $L=L_0+2\Delta L$	20
13 Differential RF Insertion Phase for the Longest Delay-line Combination of $L=L_0+15\Delta L$	21
14 Photograph of Components Inside the Silica-waveguide Optical Time-shift Module	22
15 Photograph of Silica-Waveguide Time-shift Module from the Outside	22
16 Synthesized Pulse Response of Four Delay-lines After Packaging for ystem Insertion. The Measured Time-Delays are Indicated by Arrows	23
17 Plot of the Measured Time-delay vs Bit Address for the 4-bit Time-shifter	24
18 Back View of the 2-D Photonic Conformal Phased Array	25
19 Broadside Patterns Obtained on (a) Transmit and (b) Receive.....	26
20 Transmit Patterns Obtained for (a) -30° and (b) +30° Scan.....	27
21 Receive Patterns Obtained for (a) +30° and (b) +60° Scan	27
22 Photograph of the Waveguide-module with "Folded-chips"	28

TABLES

	Page
1 Key Design Parameters for Integrated Time-Delay Networks	2
2 Comparison of Waveguide Loss for High- and Low- Δn Silica-waveguides	10
3 Optical Insertion Loss of Silica Waveguide Network	19
4 Optical Insertion Loss of Folded-Chip Silica Waveguide Network	28

SECTION 1

EXECUTIVE SUMMARY

The objective of this program was to demonstrate and package a silica-waveguide time-delay network so that it can be evaluated in a phased array testbed. In particular, its target of insertion was the 96-element ARPA/Rome conformal array (developed under Contract No. F30602-91-C-006) that operated at L-band. Using an optoelectronic-switching scheme, we successfully demonstrated a 4-bit programmable time-shifter that provided time-delay steps (Δt) of 0.248 nsec. The waveguide-module was integrated into a subsystem that consisted of semiconductor lasers and detectors, RF transfer-switches, low noise RF amplifiers (LNA), and T^2L circuitries installed to enable switching of the active optoelectronic components. With the silica-waveguide module controlling one of the central columns in the conformal array, we were able to demonstrate antenna patterns that exhibited (i) a better than 50% instantaneous bandwidth and (ii) sidelobe suppression ratios of more than 10 dB (for scan angles as wide as $\pm 60^\circ$).

The organization of this final report is as follows. Section 2 gives a brief review of the technical background for this work. In particular, it discusses and compares the key design parameters for silica-based and GaAs-based integrated time-delay networks. We will then describe, in Section 3, the design of the silica-waveguide time-shifter. This includes a discussion of (i) the bending losses in curved optical waveguides, (ii) the architecture of our optoelectronic-switching scheme, and a description of the waveguide-delay-line design. The characterization of the silica-waveguide module is described in Section 4. Data from measurements of the optical insertion loss, the RF-insertion phase, and the time-domain response will be presented in this section. Finally, we will present (in Section 5) the results obtained from its evaluation in the ARPA/Rome conformal array. We will also summarize the accomplishments of our program in this section.

SECTION 2

INTRODUCTION

Since the first demonstration⁽¹⁾ of an optical steered phased array antenna, many architectures for implementing optical beam-forming networks have been proposed and realized⁽²⁾. Among the reported schemes, those offering true-time-delay (TTD) still has the best potential for meeting future needs in multifunction and multiband operations, especially over wide scan angles. Thus far, the photonic time-shift modules demonstrated for system insertions were all composed of fiber-based delay-lines, whose lengths were trimmed individually to meet specific time-delay requirements, as dictated by the aperture size and steering angle of the array. An integrated *waveguide-based* delay-line technology offers several advantages over their fiber-based counterparts. First, the waveguides are typically fabricated by photolithographic processes with dimensional precisions of micrometers. This enables better differential phase accuracy to be achieved, especially for the fine bits of the time-shifter. Although there is an initial investment for the photomask design, subsequent reproduction of identical sets of delay-lines becomes more efficient and precise with the waveguide-based technology. Secondly, the time-delay module can be packaged more compactly if the waveguide-waferboard can be adopted, in addition, as a monolithic or hybrid integration platform for the active components.

In Ref. 3, we reported a detector-switched monolithic GaAs time-delay network with 2-bits of resolution. Because silica-waveguides typically demonstrate a propagation loss of less than 0.1 dB/cm, they are a more attractive choice for steering phased arrays with large aperture sizes and wide scan angles. In Table 1, we compare the key design parameters for silica- and GaAs-based integrated time-delay networks.

Table 1. Key Design Parameters for Integrated Time-Delay Networks.

	Si	GaAs
Substrate	~4" (6" max)	2"
Waveguide Material	Ge-Doped Silica (Buried)	GaAlAs/GaAs (Rib)
Loss (dB/cm) (For Curved Guides)	~0.1	~1
Refractive Index (n)	~1.5	~3.45
Loss per nsec of Delay	~2 dB	~8.7 dB
Minimum Bend Radius	~5 mm ($\Delta n/n \sim 0.65\%$)	~3 mm ($\Delta n/n \sim 2\%$)
Fiber Coupling	~-0.5 dB	~-3 dB
Device Integration	No (Hybrid Platform)	Detector Switch (>40 dB Isolation)

The silica waveguides are composed of a Ge-doped SiO_2 core ($6 \mu\text{m} \times 6 \mu\text{m}$) embedded inside SiO_2 (see Figure 1). These core and cladding layers are deposited by flame hydrolysis on Si substrates that are typically four inches in diameter. On the other hand, the waveguides for the GaAs-based technology are of the rib-type (see Figure 2). The epitaxial layers from which these rib-waveguides are fabricated are grown by MOVPE on GaAs substrates that are typically \sim two inches in diameter.

9327-32-041

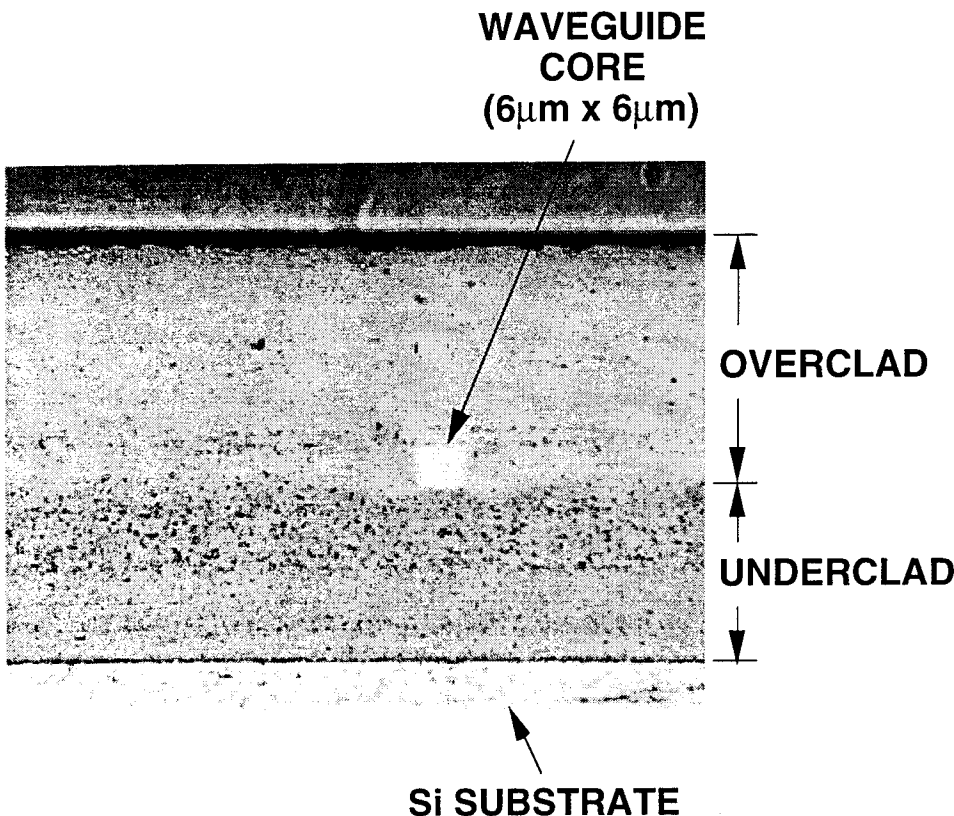


Figure 1. SEM Micrograph of Buried Silica-waveguide.

We show, in Figure 3, the fabrication sequence of the buried silica waveguides by flame hydrolysis (FHD). Partially because they are buried waveguides, the propagation loss of straight silica waveguides is only 0.04 dB/cm (for those with $\Delta n/n \sim 0.65\%$, n =index of refraction). This figure is to be compared with typical losses of ~ 0.5 dB/cm for straight GaAlAs/GaAs rib-waveguides.

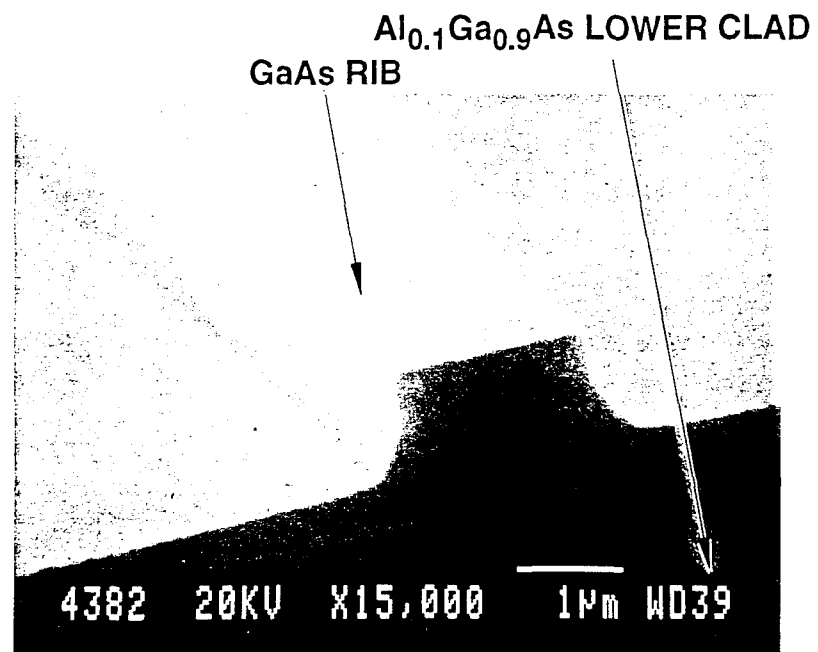


Figure 2. SEM Micrograph of GaAs/GaAlAs Rib Waveguide.

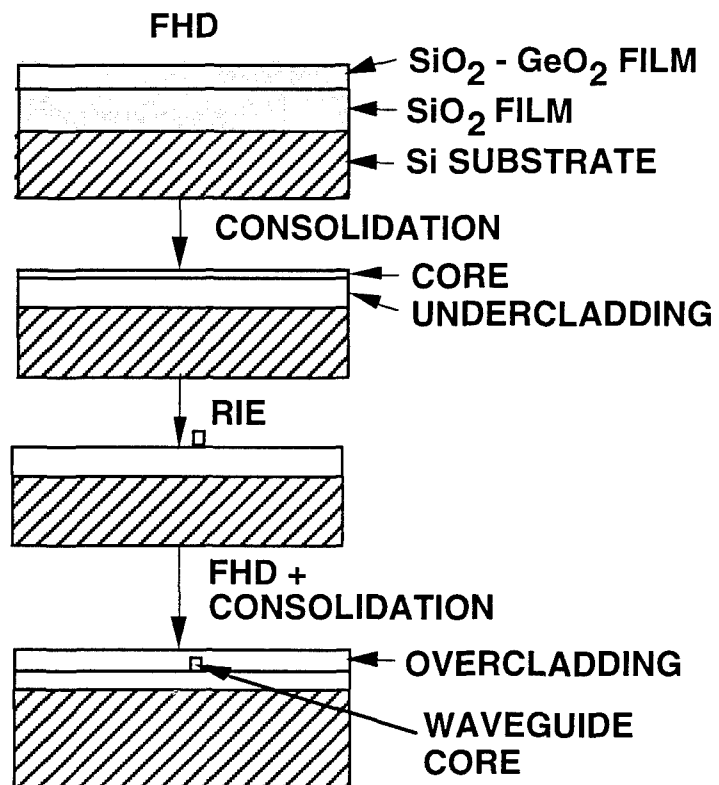


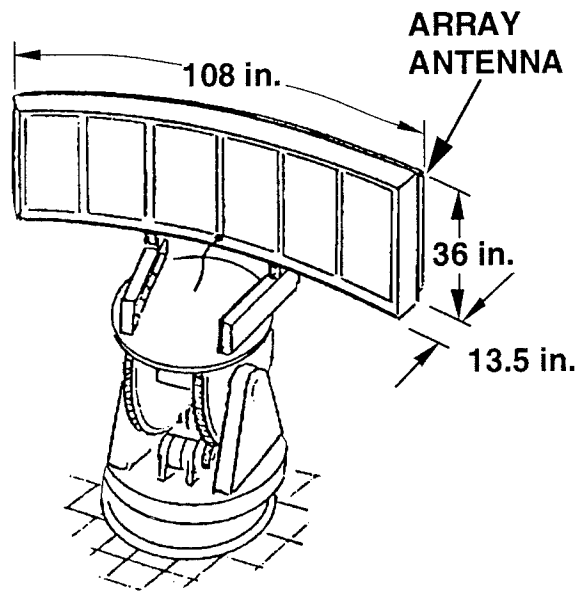
Figure 3. Fabrication Sequence of Buried Silica Waveguides by Flame Hydrolysis (FHD).

Next, because the refractive index difference between cladding and core ($\Delta n/n \sim 0.65\%$) is smaller for the silica waveguides than for their GaAs counterparts ($\Delta n/n \sim 2\%$), the minimum bend radius (R_{\min}) of silica guides, at $R_{\min} \sim 5$ mm, is slightly larger. The fact that silica waveguides cannot be “bent as tightly” as GaAs waveguides is compensated by the availability of larger Si-substrates. The typical losses of silica (high Δn type) and GaAs curved waveguides with radii of curvature approaching their bend minimums are, respectively, ~ 0.1 dB/cm and ~ 1 dB/cm. However, a more meaningful figure of merit for comparing their losses (in the context of a time-delay network) is the loss incurred for generating 1 nsec of time-delay. Because GaAs has a higher refractive index of 3.45 (vs $n=1.5$ for silica), it can generate more time delay ($\Delta t = nL/c$) per unit length (L) than silica. Taking into account the loss per unit length and the time-delay per unit length, we obtain a propagation loss of ~ 2 dB/nsec for silica waveguides vs. ~ 9 dB/nsec for GaAs rib waveguides. In addition, silica waveguides demonstrate a lower coupling loss (of only 0.45 dB, i.e., $\sim 10\%$) to single mode fibers than GaAs waveguides. This is because the core/clad of the single-mode silica waveguides are very similar in refractive indices and physical dimensions to optical fibers. This, in turn, reduces the mode-mismatch between the optical fiber and silica waveguide. However, a GaAs-based technology allows the detector switches to be *integrated monolithically* with the waveguide-delay lines. This not only enables the time-delay network to be packaged more compactly, but also eliminates an extra coupling interface between the delay-lines and optoelectronic switches. Finally, the optical input to a GaAs integrated time-shift network is distributed to its delay branches by cascaded Y-branch ($1 \times N$) splitters. In contrast, $N \times N$ star-couplers based on a Fourier optics design are used in a silica-based network to distribute the optical inputs. As we shall see, the latter design would enable the implementation of higher bits of resolution without incurring excess splitting loss.

In this program, the *target of insertion* for the integrated optical time-delay network was the ARPA/Rome conformal array⁽⁴⁾ (see Figure 4) that operates at L-band (~ 850 -1500 MHz). Populated by 96 ($= 24 \times 4$) radiating elements, the aperture of the two-dimensional array was ~ 1 m \times 2.7 m. In particular, these radiating elements were grouped into 24 columns and arranged to lie on an arc with a radius of curvature equal to ~ 3.05 m. Inside the conformal array, the 24 columns were further grouped into 8 subarrays, each of which was designed to be steered by a photonic time-shifter.

Specifically, the targets of insertion for the waveguide-based time-delay network were the central subarrays of the antenna. For these central columns, a 4-bit time-shifter that provides quantized time-delays of 0, Δt , $2\Delta t$,.. to $15\Delta t$ is sufficient to satisfy the scan-angle requirements of $\pm 60^\circ$. However, because of the large aperture size and wide scan-angle requirement for this antenna, the step-size (Δt) for the quantized delay-times must be 0.25 nsec. This implied that we

(a)



(b)

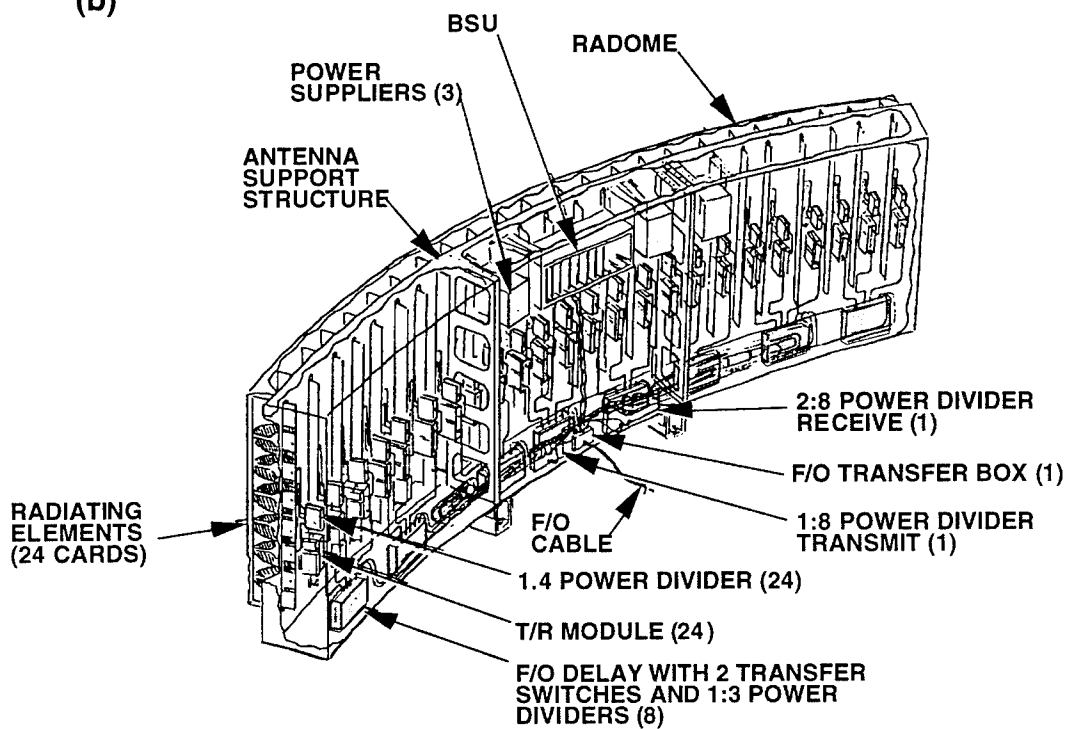


Figure 4(a). Outer Dimensions of the ARPA/Rome L-band Conformal Array;
4(b) The Antenna Aperture and Beam-forming Network of the Array.

need to generate a time-delay of 3.75 nsec (from the waveguide-module) for the longest time-delay option of $15\Delta t$. Thus, a GaAs-based time-delay network would require a delay-line that is as long as 32.6 cm - a length that could incur a fairly high insertion loss of ~ 33 dB. Consequently, we decided to pursue the development of a silica-based optical time-shift network to accomplish our system insertion goals. Using a time-delay of ~ 50 psec/cm for silica-waveguides, we estimated that we need a maximum delay-length of 75 cm (for the delay-option of $15\Delta t$) in a silica-based time-delay network.

SECTION 3

DESIGN OF 4-BIT OPTOELECTRONIC-SWITCHED SILICA-WAVEGUIDE TIME-SHIFTER

To generate the time-delays necessary to steer the 96-element conformal array, we need to design and integrate waveguide-delay-lines with length differences of ΔL , $2\Delta L$, $3\Delta L$..and $15\Delta L$, where $\Delta L=5$ cm, on silica-waveguide chips. Since the silicon substrates on which these delay-lines are fabricated have a finite area (~ 4 " in diameter), the optical waveguides need to be *curved* so that compact "loops" with pre-designed geometries can be formed for them on the finite real estate of the Si-substrate. Unfortunately, the bending of these waveguides incurs optical losses in their guided modes. In Section 3.1, we will discuss the origin of these bending losses. An understanding of these bending losses provides the basis for laying out the mask sets used to fabricate the integrated delay-lines.

In Section 3.2, we will discuss the architecture of our "optoelectronic-switched" time-delay network. In this switching scheme, the delay-path of the optical carrier (for the RF) is *defined* by turning on a laser and detector located, respectively, at the beginning and end of an analog optical link. As we shall see, by combining laser- and detector- switching, we were able to divide the integration of the above delay-lines into two silica-waveguide chips, with one chip hosting the shorter delay-lines (reference line 1, ΔL , $2\Delta L$, $3\Delta L$), and a second chip hosting the longer delay-lines (reference line 2, $4\Delta L$, $8\Delta L$, $12\Delta L$).

Finally, in Section 3.3, we will describe the actual geometric layout of the integrated delay-lines on the two chips. In comparison with conventional microwave guides such as RF-striplines, the following technical attributes of the optical waveguides offered significant advantages for realizing a miniature time-delay network. First of all, these optical waveguides demonstrate excellent optical confinement. Therefore, they can be spaced as close as ~ 100 μm apart without fear of RF-crosstalk. This enabled us to pack these delay-lines into compact "loops" with precisely designed physical lengths. Secondly, these optical waveguides can intersect at right angles with virtually no cross-coupling in optical energy. This helped us to lengthen the delay-lines within the confines of a 4-inch diameter Si substrate. The above two attributes are unique to these optical waveguides, and are difficult to attain with conventional microwave strip-line technology. In particular, they serve to illustrate the advantages of adopting a photonic time-delay network.

3.1 BENDING LOSSES OF CURVED INTEGRATED OPTICAL WAVEGUIDES

In this section, we will present the equations that dictate the bending loss of the integrated optical waveguides. As we shall see, these equations show that the bending loss decreases exponentially as the bend's radius of curvature increases. Figure 5 shows a guided mode propagating around a waveguide bend from a straight waveguide section. The transition between the straight and curved waveguide sections is indicated by a dotted line that is coincidental with the phase front of the incident mode to its left. As shown, most of the optical power in the guided mode is confined inside the waveguide-core with refractive index n_1 . However, it does have an evanescent tail, characterized by a decay constant α_x , in the waveguide clad with index n_2 . To be specific, a well-confined optical mode has a large decay-constant α_x and a short evanescent tail given by $\exp(-x\alpha_x)$, where $|x| > (d/2)$, the half-width of the waveguide-core. We will show later that the magnitude of α_x has a direct impact on the bending loss of the curved optical waveguide.

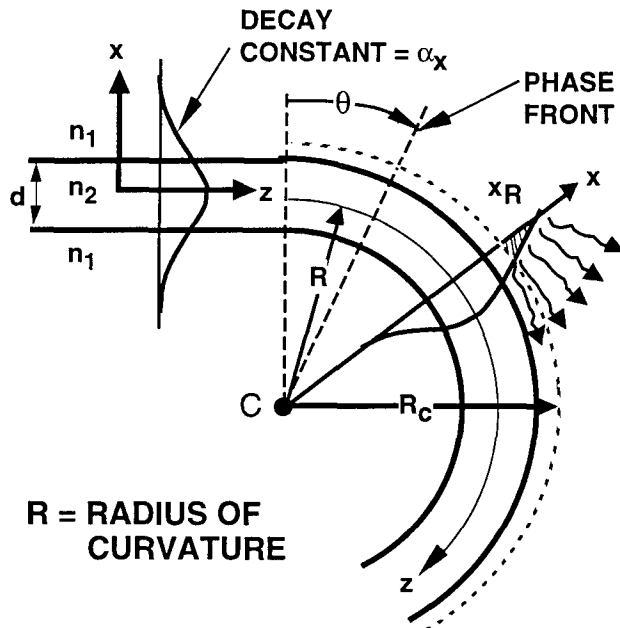


Figure 5. Radiation Loss from an Optical Mode Guided Around a Waveguide Bend.

The origin of the bending loss is as follows. As the optical mode moves around the bend, its phase front (indicated by the dotted line) must rotate about its center of radius of curvature C. We see immediately that the path length (d) of the trajectory for an infinitesimal portion (dx) of the mode increases with its distance r ($r = R + x$) from C, where R denotes the bend's radius of curvature. Specifically, if θ is the angular rotation of the phase-front, $d = \theta \times r$. This implies, in

particular, that the outer evanescent tail (with larger r) must travel faster than the inner evanescent tail to keep the same angular rotation. Since the maximum speed at which any part of the mode can travel is the velocity of light ($= c/n_1$) in the outer clad, the part of it that lies beyond a critical radius R_c would not be able to “keep up” with the rest of the mode as it goes around the bend. A simple estimation shows that R_c is given by $R_c = (n_{\text{eff}}R)/n_1$, where n_{eff} is the effective index of the waveguide mode. This portion of the mode (indicated as the shaded portion in Figure 5) is effectively radiated from the guide in a distance of $z_c \sim (\lambda_1 \alpha_x^2)^{-1}$, where $\lambda_1 = \lambda/n_1$ is the optical wavelength in the medium n_1 . By computing the mode-energy inside the shaded portion of the mode, we obtain the following expression for the radiation loss of the curved waveguide per unit length:

$$\alpha_r = c_1 \exp(-c_2 R) \quad (1)$$

where $c_1 = \alpha_x^2/k_1$, and $c_2 = \alpha_x^3/k_1^2$. In the above equations, $k_1 = (2\pi)/\lambda_1$. The radiation loss given by Eq.1 is fundamental to the propagation of optical modes around waveguide bends. It occurs in bends formed by loops of optical fibers as well as those formed by integrated delay-lines on a chip. The dominant term on the right hand side of Eq.1 is the term in the exponential. As the equation shows, the radiation loss α_r decreases exponentially with c_2 , a parameter that is proportional to α_x^3 . Thus, a well-confined mode with a *larger* α_x will demonstrate a *smaller* bending loss. For optical waveguides with approximately the same core width d , α_x is determined, to a large extent, by $\Delta n/n_2$, where $\Delta n = n_2 - n_1$. In particular, a higher Δn gives rise to better mode-confinement, and enables a larger α_x to be obtained. Finally, the radiation loss coefficient α_r *decreases* with the radius of curvature R . Thus, a gentle bend in the integrated delay-lines induces less loss than a bend with a sharp-turn.

In Table 2, we compare the dependence of the measured waveguide loss on the two parameters, α_x and R , for two types of silica-waveguides.

Table 2. Comparison of Waveguide Loss for High- and Low- Δn Silica-waveguides.

Waveguide Type	$\Delta n/n$ ($n \sim 1.5$)	Core Size	Fiber Coupling Loss	Minimum Bending Radius (R_{min})
Low- Δn	~0.3 %	8 $\mu\text{m} \times 8 \mu\text{m}$	0.2 dB (=4%)	25 mm
High- Δn	~0.65 %	6 $\mu\text{m} \times 6 \mu\text{m}$	0.45 dB (=10%)	5 mm

As shown in the Table 2, we classify the silica waveguides into the low- Δn ($\Delta n/n \sim 0.3\%$) and the high- Δn ($\Delta n/n \sim 0.65\%$) types. Although the core of the low- Δn waveguide can be as wide as 8 μm and yet maintain single mode propagation, its minimum bend radius of curvature ($R_{\text{min}} \sim 25$ mm) for achieving an acceptable bending loss is noticeably larger. This is to be compared with a waveguide core of 6 μm and an R_{min} of ~5 mm for the high- Δn silica-

waveguides. However, one can obtain a lower fiber-coupling loss (of ~ 0.2 dB) for the low- Δn type waveguide. Because rather long delay-lengths were needed to steer the 96-element array through scan angles of $\pm 60^\circ$, we decided to adopt the high- Δn waveguides in our design.

Once the decision to adopt the high- Δn waveguides was made, α_x was fixed by the choice of n_1 , n_2 , and the waveguide-dimensions of $\sim 6 \mu\text{m} \times \sim 6 \mu\text{m}$ designed to maintain the propagation of only the fundamental mode in the waveguides (see Figure 1). The radius of curvature R then became the key design variable for laying out the geometry of the integrated delay-lines. As mentioned above, the minimum bend radius of curvature for these “high- Δn ” silica-waveguide is ~ 5 mm. By adopting bend radii of curvature larger than 6.7 mm, we were able to fit all the delay-lines inside silica chips $\sim 6 \text{ cm} \times \sim 7 \text{ cm}$ in size.

Aside from the fundamental radiation loss discussed above, the guided mode also suffers a small transition loss at junctions that join together waveguides with dissimilar radii of curvature. This kind of coupling loss is illustrated in Figure 6 for a junction between a straight waveguide and a curved one. The origin of this transition loss is the existence of a shift in the mode’s beam-axis as it crosses the waveguide junction. As shown in Figure 6, the amplitude distribution of the mode shifts outwards as it enters the curved waveguide from the straight segment. Intuitively, we can explain the shift of the mode beam-axis by the following physical reasoning. The phase velocity for the portion of the mode in the outer clad (with index n_1) is $v_1=c/n_1$, which is larger than the phase velocity v_2 ($v_2=c/n_2$, where $n_2 > n_1$) in the waveguide-core of index n_2 . By shifting its beam-axis outwards (towards the medium with index n_1), a larger fraction of the mode-power picks up the higher phase velocity v_1 . This, in turn, enables its phase-front (shown as dotted lines in Figure 6) to tilt at an angle from the coupling plane (between the curved and straight waveguide segments), as is necessary for the mode to go around the bend. Again, this kind of shift in the mode beam-axis occurs in loops of fibers as well as in integrated waveguides fabricated on a chip. As a result of the shift, the mode profiles (indicated as “amplitude distribution” in Figure 6) become physically mismatched along the coupling plane. This mode mismatch is the source of the transition loss at the waveguide junction. For silica waveguides, the transition loss amounts to ~ 0.017 dB/junction. As a remedy to reduce this kind of transition loss, the waveguides can be offset at their junction to reduce the mismatch of the mode-profiles.

3.2 DESIGN OF 4-BIT OPTOELECTRONIC-SWITCHED TIME-DELAY NETWORK

As mentioned earlier, we varied the delay-times in our time-delay network by means of “optoelectronic switching”. In this switching scheme, the delay path of the optical carrier is defined by selectively turning on a laser and detector located, respectively, at the beginning and end of an analog optical link. Figure 7 shows the architecture of the 4-bit silica-waveguide time-delay network.

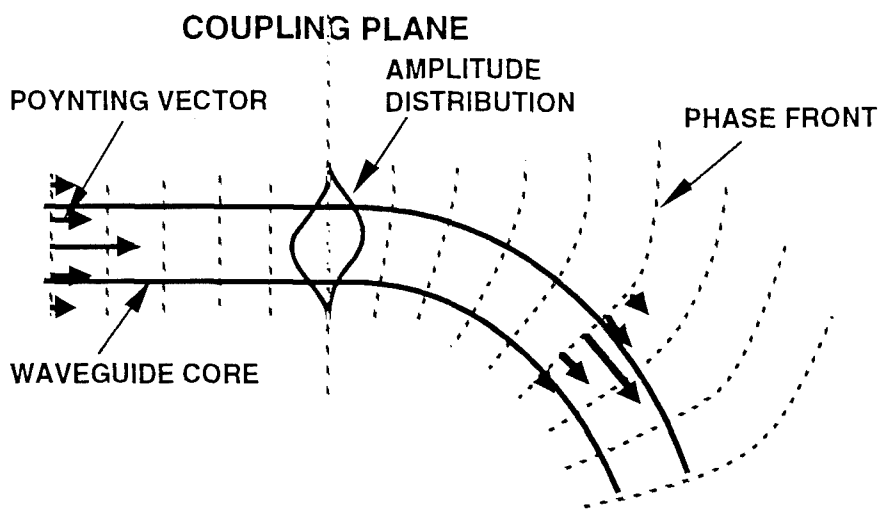


Figure 6. Transition Loss Occuring at a Junction Joining a Straight and a Curved Waveguide Segment.

9327-32-043R2

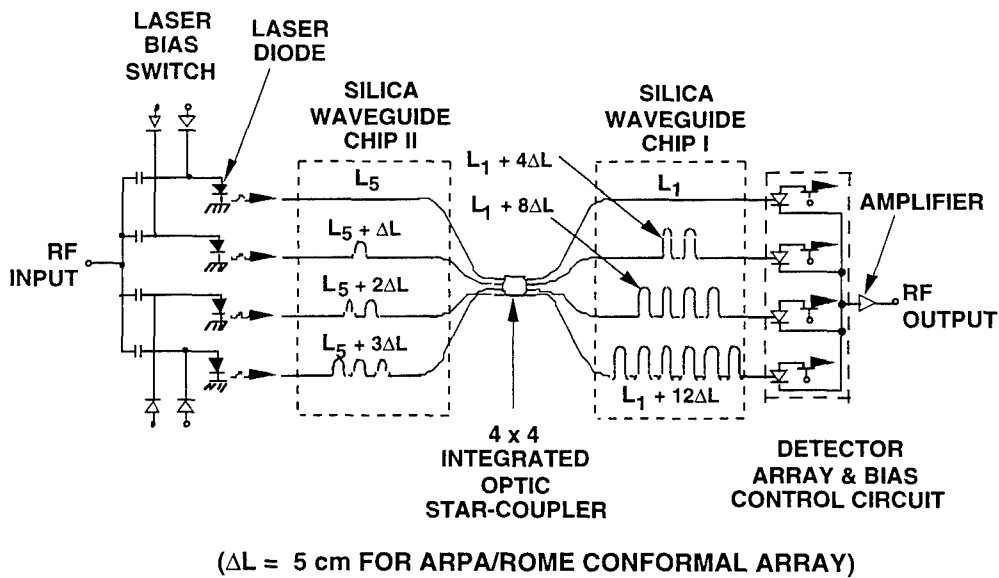


Figure 7. Schematic of 4-bit Silica-waveguide Optical Time-shift Network.

As shown in Figure 7, the delay-lines were integrated on two silica-waveguide chips (II and I), butt-coupled respectively to the input and output ends of a 4×4 silica star-coupler. The dimensions of chips I and II were $6 \text{ cm} \times 7 \text{ cm}$ and $5 \text{ cm} \times 6 \text{ cm}$, respectively. By using a "loop-type" geometry with a bend radius of curvature larger than 6.7 mm, we successfully integrated delay-lines with lengths of 7.2 cm, 27.2 cm, 47.2 cm, and 67.2 cm on chip I. Similarly, waveguide-delay-lines with lengths of 6 cm, 11 cm, 16 cm, and 21 cm were integrated on chip II.

As shown in Figure 7, four lasers were coupled to chip II. When we biased up any of the four lasers (to approximately three times above threshold), the RF input to the time-delay network was modulated onto that laser's optical output. By biasing up the appropriate laser, we selectively coupled light into one of the four shorter delay-lines on chip II (located at the input side of the star-coupler): L_5 , L_6 ($=L_5+\Delta L$), L_7 ($=L_5+2\Delta L$), L_8 ($=L_5+3\Delta L$). The optical carrier was split into four by the star-coupler, and subsequently coupled to delay-lines L_1 , L_2 ($=L_1+4\Delta L$), L_3 ($=L_1+8\Delta L$) and L_4 ($=L_1+12\Delta L$). We then selectively detected one of these four optical branches by “switching” on the photodiode pigtailed to the appropriate delay-line. In practice, this was accomplished by turning-off the voltage applied to the gate of a GaAs MESFET (“normally on”) connected in series with the photodiode (see Figure 7). For example, by selecting the laser pigtailed to L_7 and the detector pigtailed to L_3 , we obtained, at the RF output, a microwave signal that had been routed through a delay-path with a differential delay length of $10\Delta L$. Thus, laser-switching controlled the time-delays corresponding to the two finer bits of the four, whereas detector-switching controlled the two most significant bits. Combining laser and detector switching, the network of Figure 7 provided 16 delay options (i.e., four bits of resolution) from L_0 ($=L_1+L_5$) to $L=L_0+15\Delta L$. The optical losses of such a time-delay network consisted of (i) a fan-out loss of ~ 8 dB (at the 4×4 star-coupler), (ii) interface-coupling losses (of 0.5 dB/interface) between the silica-chips, and (iii) propagation losses in the silica-waveguides. In Section 4, we will present the results of the optical loss measurements for all the delay-line combination [L_i ($i=5..8$) to L_j ($j=1..4$)] from the two waveguide-chips.

3.3 DELAY-LINE DESIGN FOR THE 4-BIT SILICA-WAVEGUIDE TIME-DELAY NETWORK.

As described in the last section, the four waveguides for the two minor bits of the four-bits - L_5 , L_6 , L_7 , L_8 - were integrated on chip II with a dimension of ~ 5 cm \times 6 cm. This chip was butt-coupled to the input end of a star-coupler fabricated on another silica-waveguide chip ~ 1.5 cm \times 2 cm in size. The output end of the star-coupler was finally butt-coupled to silica-waveguide chip I that contained the delay lines L_1 , L_2 , L_3 and L_4 . As shown in the waveguide layout of Figure 8, the size of this chip (chip I) was ~ 5 cm \times 6 cm. We expected the coupling loss of each butt-joint to be less than 0.5 dB (i.e. $<11\%$). Potentially, the star-coupler could be integrated with chip II to further reduce the size of the photonic time-shifter. However, this was not pursued so that a prototype that was ready for system insertion could be demonstrated within the program time-frame.

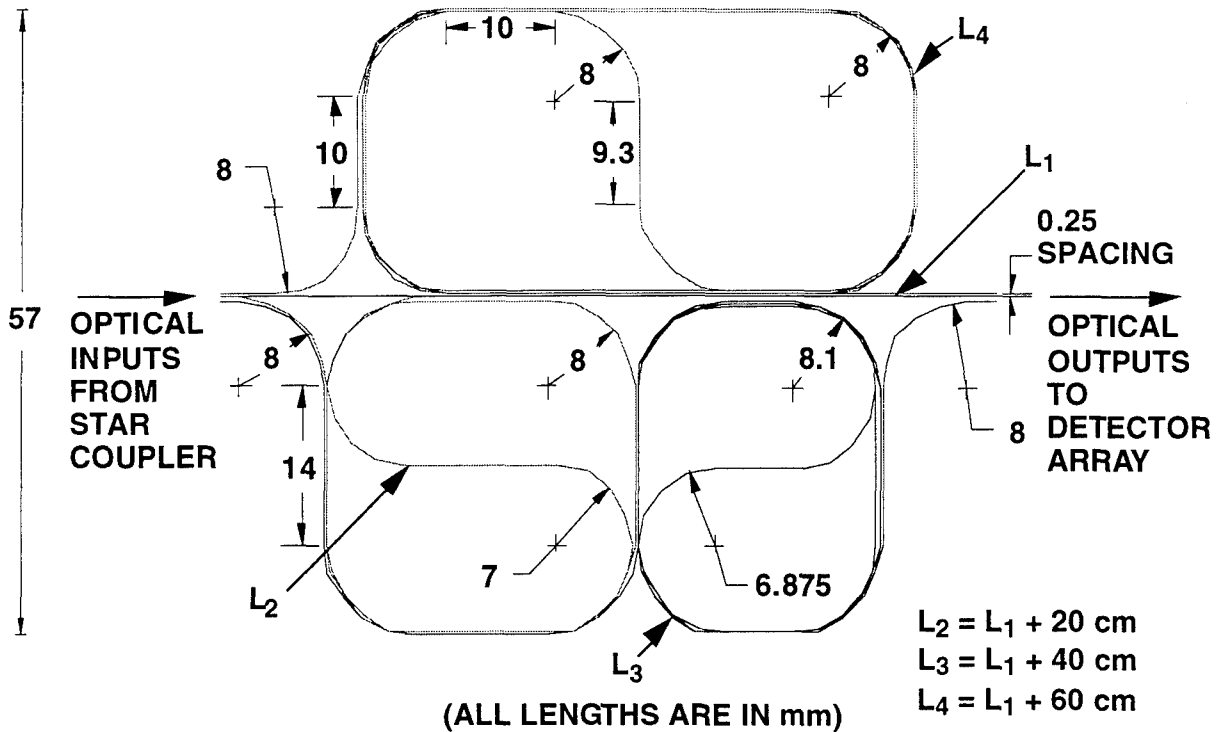


Figure 8. Waveguide Layout of Chip I.

As mentioned in Section 3.1, the curved waveguides of chips I and II were designed to be high- Δn silica waveguides with bend radii larger than 6 mm. We expected the propagation losses of these curved waveguides to be $\sim 0.1 \text{ dB/cm}$. The 4×4 star coupler was expected to incur an intrinsic splitting loss of 6 dB and an excess loss of 2 dB. Taking into account the propagation loss, the splitting loss at the star coupler and the butt-joint loss, we expected an average loss of $\sim 15 \text{ dB}$ between the input and output ends of the waveguide network.

The layout of waveguide chip I is shown in Figure 8. In Figure 9, we show the detailed geometric design used to generate the waveguide “loops” of chip I. We derived formulas for the differential delay lengths (ΔL_d) of two types of delay-line designs: (i) Type I used for delay lines L_2 and L_3 , and (ii) Type II designed for L_4 . Specifically, if N is the number of complete clockwise and counter-clockwise loops, then ΔL_d for the type I design is given by:

$$\Delta L_d = (N + 1)2\pi R + (\pi - 4)r + 2(N + 1)(S_1 + S_2) - \Delta R[(N^2 - \frac{1}{2})\pi + 4N + 2]$$

where R , r , S_1 , S_2 and ΔR are labelled in Figure 9. A similar equation was also derived for the type II curves. Specifically,

$$\Delta L_d = 2N(S_1 + S_2) + 2S_1 + (2N + 1)\pi R + (\pi - 4)r - \Delta R[4N - 2 + N(N - 1)\pi]$$

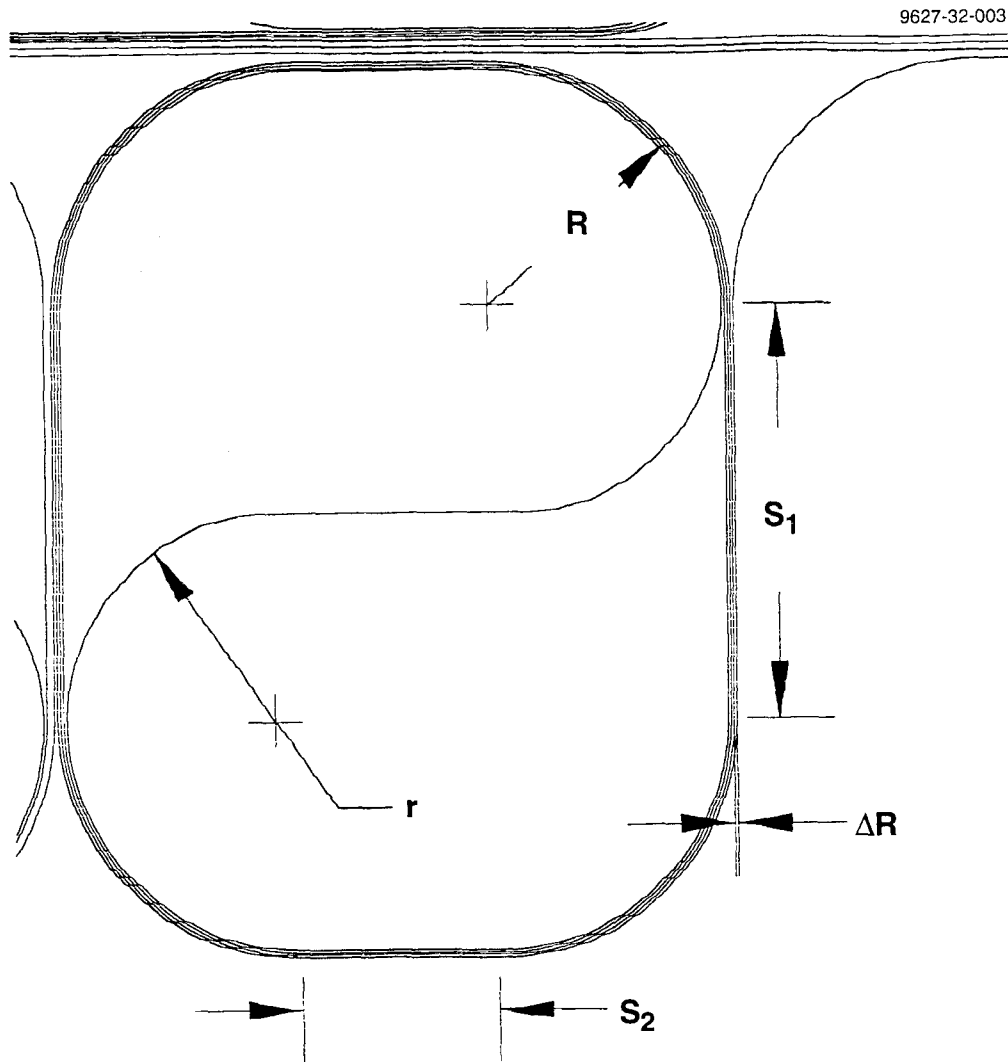


Figure 9. Waveguide "Loop" in Chip I.

Figure 10 shows the geometric layout for the waveguides used in chip II. As illustrated, waveguide "cross-overs" at right angles were used for delay-lines L₇ and L₈. A detailed analysis showing that there is negligible coupling between the two intersecting waveguides is given in Ref. 5. Finally, we submitted the above waveguide designs to Photonic Integration Research, Inc. (PIRI), Columbus, Ohio for fabrication into custom waveguide chips. In the next section, we will describe the characterization of the silica-waveguide time-delay network.

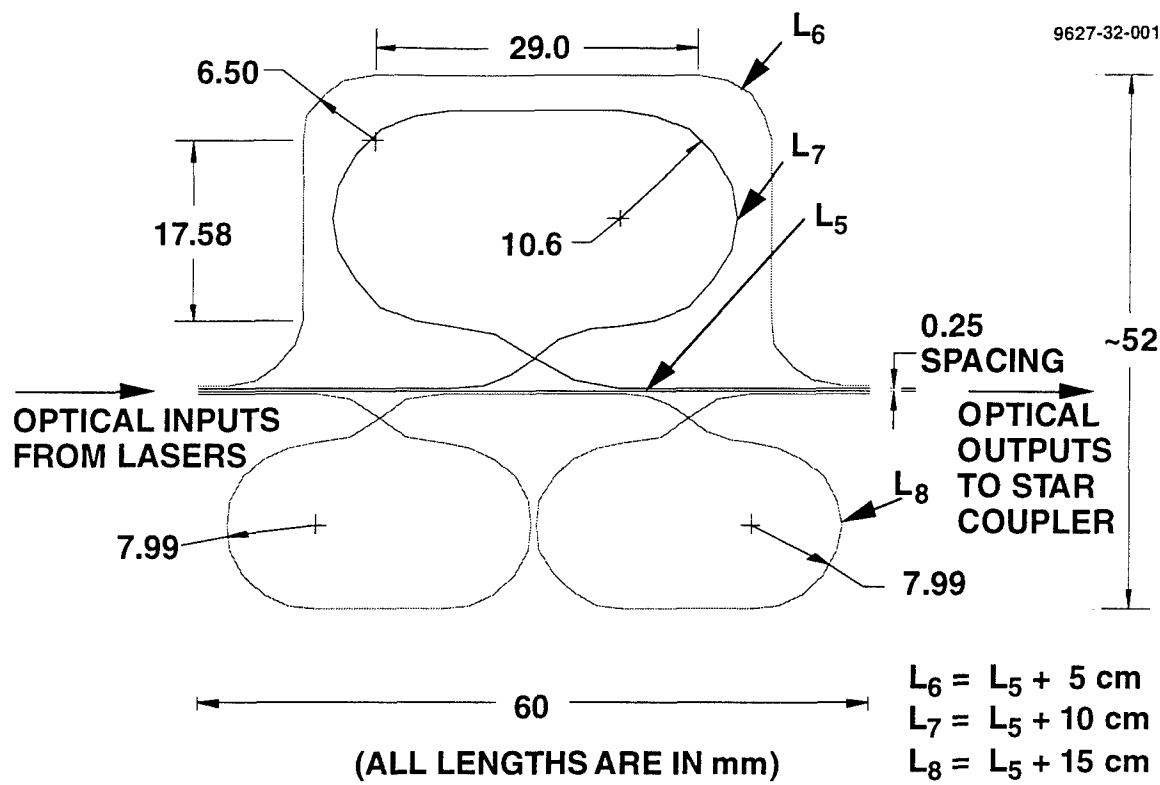


Figure 10. Waveguide Layout of Chip II.

SECTION 4

CHARACTERIZATION OF THE SILICA-WAVEGUIDE OPTICAL TIME-SHIFT NETWORK

In this section, we will describe the characterization of the silica-waveguide optical time-shift network. After the silica-waveguide chips were fabricated, we first measured the optical insertion loss of each delay path. We present the results of these DC measurements in Section 4.1. With the help of a microwave network analyzer (HP8510B), we then characterized the waveguide network by measuring (i) the differential RF insertion phase between its input and output ports, and (ii) its synthesized pulse response. From either of these measurements, we can deduce the time-delays generated for each delay-line combination in the waveguide-network. The RF insertion phase data presented in Section 4.2 were obtained before the waveguide-network was packaged for system insertion. On the other hand, the data for the synthesized pulse responses (Section 4.3) were taken after the waveguide-network was integrated with other RF-components in a ruggedized module.

4.1 MEASUREMENTS OF THE OPTICAL INSERTION LOSS

Figure 11 shows a photograph of the waveguide-chips after they were fabricated and butt-coupled to each other. We first characterized the optical insertion loss of each delay-path (from $L_o, L_o+\Delta L, L_o+2\Delta L, \dots$ to $L_o+15\Delta L$). These results are tabulated in Table 3. In this Table, the first row designates the delay-lines ($L_i, i=5..8$) fabricated on chip II. The numbers shown in brackets in this row are the physical lengths of the respective waveguides on this chip. As mentioned in Section 2, the difference in length between these delay lines increases in steps of $\Delta L=5$ cm. Similarly, the delay-lines ($L_j, j=1..4$) on chip I are tabulated in the first column of Table 3. The difference in physical length between these delay-lines was designed to increase in steps of $4\Delta L=20$ cm. Inside the table, we have a matrix (M_{ij}) that shows the measured optical loss (L_t) of different delay-line combinations, each consisting of a delay-line from chip I and chip II [i.e. connecting L_i ($i=5..8$) to L_j ($j=1..4$)]. For example, the matrix element M_{11} gives the measured loss of the delay-path connecting L_5 to L_1 . As tabulated, L_t equals 12.12 dB in this delay-path. The number tabulated in brackets in the matrix is the estimated loss per unit length (α) of each delay-path combination. As an example, the number inside the brackets in M_{11} gives a loss per unit length of 0.05 dB/cm for the delay-path combination of L_5 and L_1 . Below, we detail how α is evaluated.

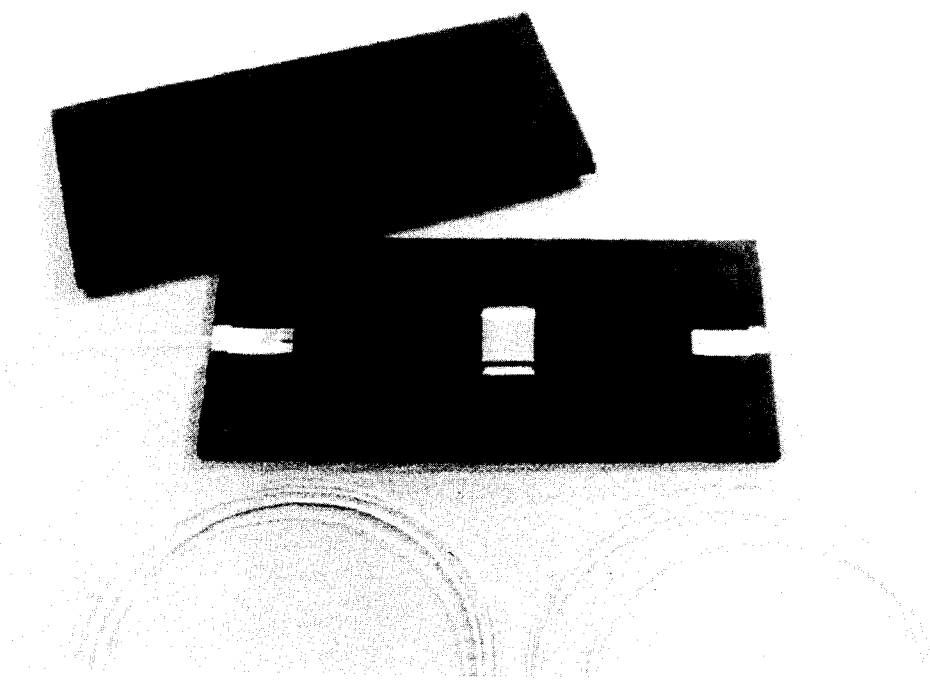
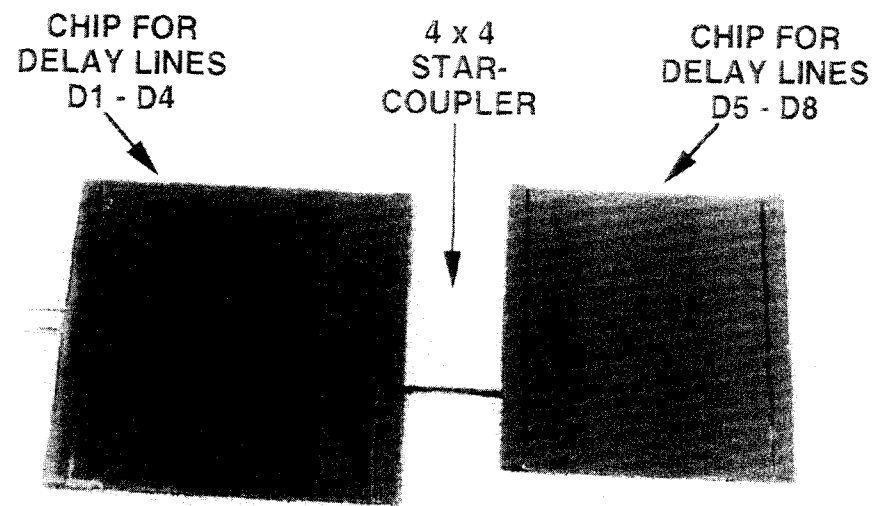


Figure 11(a). Photograph of Silica Waveguide Chips I and II Butt-coupled Against 4×4 Star-coupler; (b) Photograph of Al-housing and Fiber-pigtails for the Waveguide Chips.

Table 3. Optical Insertion Loss of Silica Waveguide Network.

L_t in dB (α in dB/cm)	L_5 (6 cm)	L_6 (11 cm)	L_7 (16 cm)	L_8 (21 cm)
L_1 (7.2 cm)	12.12 (0.05)	13.20 (0.09)	13.13 (0.07)	13.32 (0.06)
L_2 (27.2 cm)	13.76 (0.07)	14.16 (0.07)	14.23 (0.06)	15.16 (0.08)
L_3 (47.2 cm)	16.12 (0.09)	17.35 (0.1)	16.50 (0.08)	17.07 (0.08)
L_4 (67.2 cm)	17.04 (0.08)	17.80 (0.08)	18.14 (0.08)	19.23 (0.09)

The optical loss L_t that we measured experimentally consisted of (i) the fan-out loss (L_f) of the 4×4 star-coupler, and (ii) interface coupling losses (L_{cp}) between the butt-coupled chips, and (iii) propagation losses (L_{prop}) in the silica waveguides. For a 4×4 star-coupler, the intrinsic splitting loss is 6 dB. Adding an excess splitting loss of ~ 2 dB to the above intrinsic splitting loss, we obtained $L_f \sim 8$ dB for the fan-out loss. The interface coupling loss was ~ 0.5 dB/interface. On top of that, there was a bonding loss of ~ 0.375 dB/interface. Since there were 4 interfaces (fiber-pigtail to chip and chip to star-coupler) for each delay-line combination, L_{cp} amounted to 3.5 dB in total. Finally, the propagation losses L_{prop} consisted of the bending losses discussed in Section 3.1 as well as scattering losses due to fabrication imperfections. By subtracting L_f and L_{cp} from the measured loss L_t , we obtained L_{prop} for a particular delay-line combination. Dividing L_{prop} by the total physical length (D) of the delay path gave us an estimation of α , the propagation loss per unit length. Hence,

$$\alpha = \frac{L_t - L_{cp} - L_f}{D}$$

As shown, the average propagation loss per unit length was only ~ 0.077 dB/cm for the waveguides in our design. The lowest value of 0.05 dB/cm for α was obtained, as expected, for the delay-line combination of L_1 and L_5 because these reference lines were straight segments. We also note from the table that the highest value for α (in the delay-line combination of L_3 and L_6) was only 0.1 dB/cm.

4.2 MEASUREMENTS OF THE DIFFERENTIAL RF INSERTION PHASE

By measuring the angular part of the scattering parameter S_{21} between the input and output ports of the waveguide-network, we obtained the RF differential phase ($\Delta\phi$) vs frequency (f) between each of the 15 delay-paths ($L_0 + \Delta L, L_0 + 2\Delta L, \dots, L_0 + 15\Delta L$) and the reference line L_0 . During these measurements, we used the same laser and detector to measure $\Delta\phi$ for each delay-line combination. Hence, the variation of the relative phase vs frequency was due entirely to the

passive network itself [i.e., the difference in waveguide length ($=m\Delta L$, $m=1\dots 15$) between the reference line and the delay-path under test]. Figure 12 shows the results of these measurements for the first two delay-lines of the fifteen.

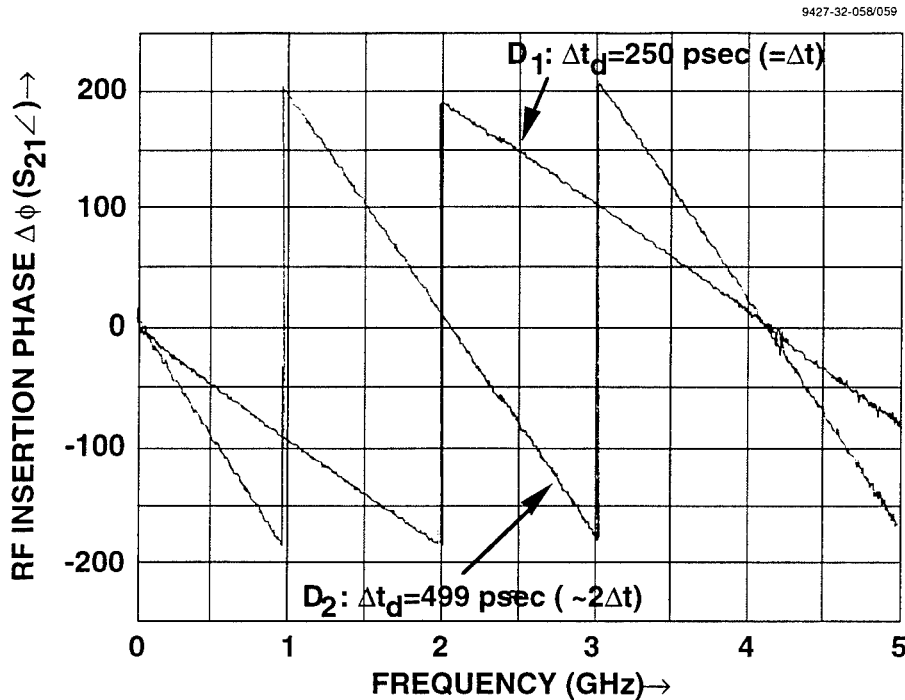


Figure 12. Relative RF Insertion Phase Vs. Frequency Between the Reference Line $L_0=L_1+L_5$ and the Delay-line Paths for (i) $L=L_0+\Delta L$, and (ii) $L=L_0+2\Delta L$.

Specifically, the difference in time delay (Δt_d) between the delay lines is given by the equation:

$$\Delta t_d = \frac{\delta(\Delta\phi)}{\delta f} \frac{1}{360^\circ}$$

Figure 13 shows the result of the relative phase measurement for the longest delay line combination of $L=L_8+L_4=L_0+15\Delta L$. These measurements showed that the measured time-delays were within ~ 15 psec of their designed value.

4.3 MEASUREMENTS OF THE SYNTHESIZED PULSE RESPONSE

After the waveguide-network was packaged into a ruggedized module for system insertion, we evaluated the complete time-shift module by characterizing its pulse response. In addition to the waveguide-network, the module contained RF transfer switches for defining the “transmit” and “receive” paths in the radar, low noise RF amplifiers, as well as T^2L circuitries installed to enable the switching of lasers and detectors. Figure 14 shows how the waveguide-network was

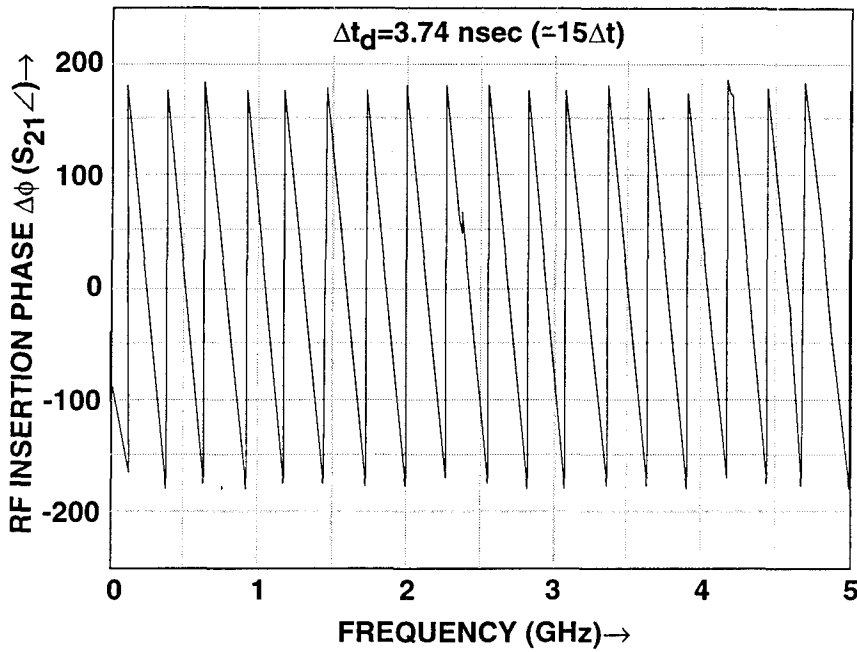


Figure 13. Differential RF Insertion Phase for the Longest Delay-line Combination of $L=L_0+15\Delta L$.

mounted on top of the active photonic components and the microwave components inside the module. A photograph of the finished module is shown in Figure 15.

To characterize the module in the time-domain, we took advantage of its broadband design (from 0.5 GHz to 1.5 GHz). With the help of the HP8510B, we first synthesized a 2-nsec-wide test-pulse from 800 (equally spaced) frequencies that lay in the 0.5-1.5 GHz frequency window. In addition, we tapered the amplitudes of these frequencies so that there were no discernible satellite peaks preceding or following the 2-nsec-wide test-pulse. To obtain the pulse response corresponding to a particular delay-path combination of L_i and L_j , we fed the synthesized pulse to the "RF input" terminal of the module. We monitored the pulse response of the system at the output terminal of the "transmit" path. Experimentally, the above objective was accomplished by measuring, one by one, the system's response to each of the 800 frequencies. These data were stored sequentially in the microwave network analyzer. Finally, an inverse Fourier transform was taken of the stored data to synthesize the desired pulse response in the time-domain. Using this technique, we can directly read off the time-delay incurred by a particular delay-path from the separation (in nsec) between its pulse response and the input test-pulse. In addition, any undesirable optical/RF crosstalk between the photonic/RF components in the module will show up as a distortion of the injected pulse. Figure 16 shows the pulse responses of four delay paths with time-delay increments of 1 nsec. As shown, the four output pulses suffered almost no distortion.

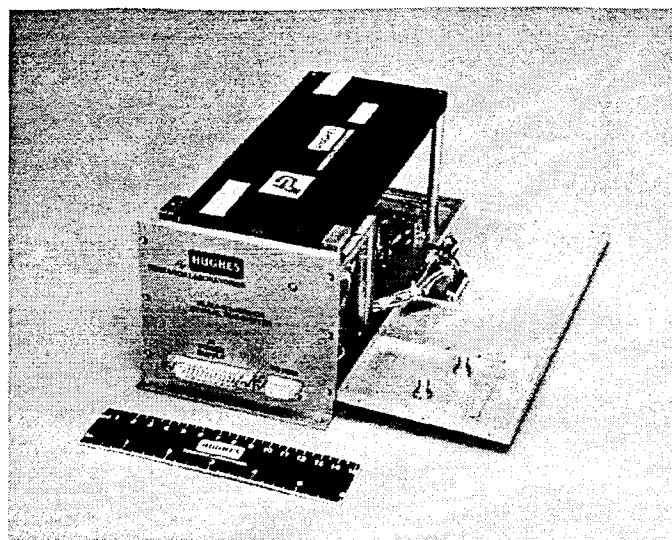


Figure 14. Photograph of Components Inside the Silica-waveguide Optical Time-shift Module.

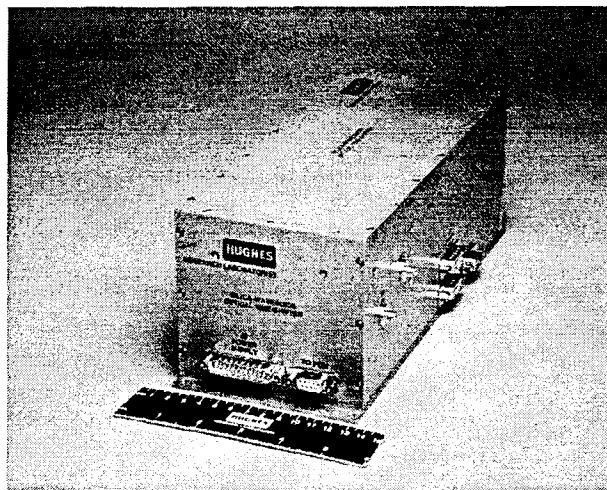


Figure 15. Photograph of Silica-Waveguide Time-shift Module from the Outside.

In Figure 17, we show a plot of the measured time-delay, as determined by the above technique, for all 16 bit-addresses of the 4-bit time-shifter. The straight line through the data points is a linear fit through the experimental data points. Specifically, the following equation gives the slope and intercept of the linear fit through the experimental data points:

$$t_d = 17.466 + 0.248 \times B$$

In the above equation, t_d is the time-delay in nsec, and B ($=1..16$) is the bit address for a particular combination of L_i and L_j .

SYNTHESIZED PULSE RESPONSE:

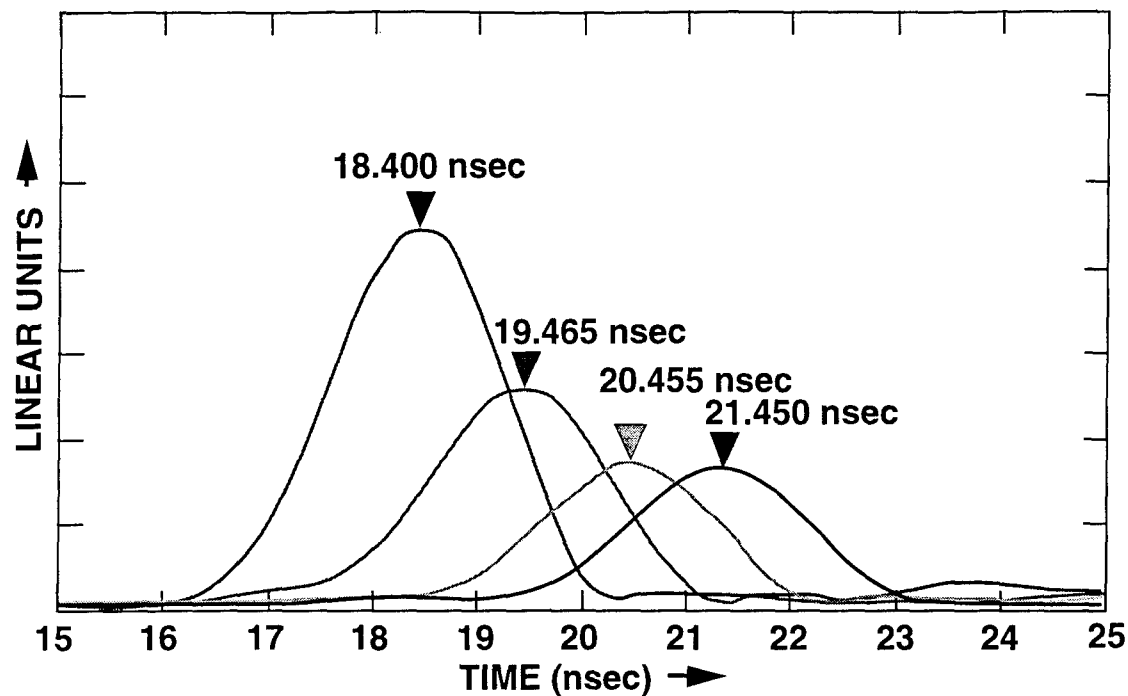


Figure 16. Synthesized Pulse Response of Four Delay-lines After Packaging for System Insertion. The Measured Time-Delays are Indicated by Arrows.

With the completion of these measurements, we inserted the module into one of the central columns of the ARPA/Rome conformal array (see Figure 4). In the next section, we will present the antenna patterns obtained with the silica-waveguide module controlling one of the central columns.

DELAY-TIME vs BIT ADDRESS

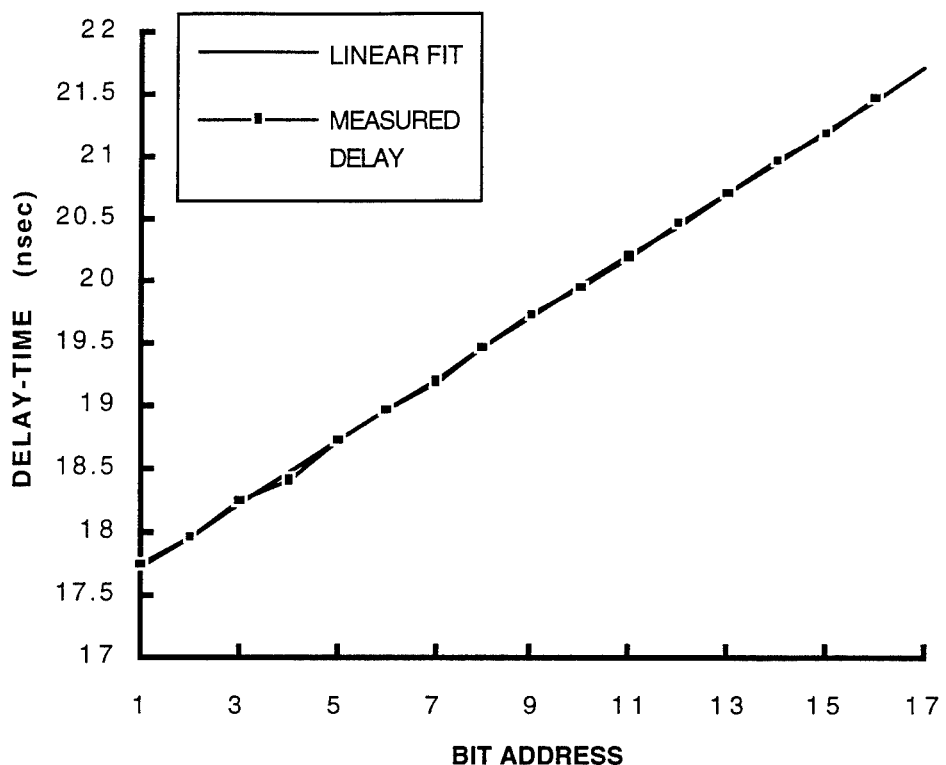


Figure 17. Plot of the Measured Time-delay vs Bit Address for the 4-bit Time-shifter.

SECTION 5

INSERTION OF SILICA-WAVEGUIDE MODULE INTO L-BAND ARRAY AND SUMMARY

In Section 5.1, we will present the results obtained from the insertion of the silica-waveguide module into the ARPA/Rome conformal array. Following that, we will describe (in Section 5.2), a “folded-version” of the waveguide network and discuss some directions for future work. Finally, we will summarize the accomplishments of our program in Section 5.3.

5.1 INSERTION OF SILICA-WAVEGUIDE MODULE INTO L-BAND CONFORMAL ARRAY

After the silica-waveguide time-delay network had been characterized, we integrated the module into the 96-element L-band conformal array (see Figure 18). As mentioned earlier, each of the eight subarrays was designed to be steered by a photonic time-shifter. In our system-insertion demonstration, one of the two central columns of the array was steered by the silica-waveguide time-shifter. The other seven subarrays were steered by photonic time-shifters that were fiber-based. Figure 18 shows the back of the antenna, where the photonic time-delay modules were located.

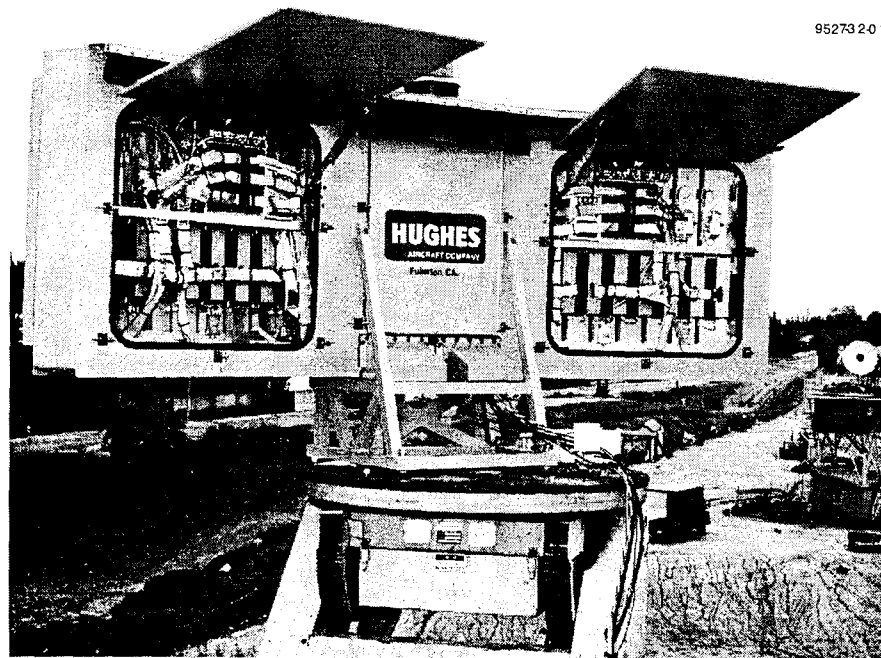


Figure 18. Back View of the 2-D Photonic Conformal Phased Array.

Figures 19 to 21 show the antenna patterns obtained with the silica-waveguide module controlling one of the two central columns of the array. Because the silica-waveguide module was a 4-bit time-shifter and the fiber-based modules were 5-bit time-shifters, the software for running the conformal array was slightly modified to accommodate the difference. In cutting these radiation patterns, the RF frequency was scanned from 0.78 GHz to 1.58 GHz, in 0.1 GHz increments. Figure 19(a) and Figure 19(b) show the broadside patterns obtained on transmit and receive respectively. As shown, the sidelobe suppression was better than 10 dB. Figure 20 plots the transmit patterns of the array for the scan angles of $\pm 30^\circ$. Finally, Figure 21 plots the patterns obtained on receive at $+30^\circ$ and $+60^\circ$. As Figure 20 and Figure 21 show, in each instance, the main beam from the array stayed steered to the prescribed angle as the RF frequency was scanned from 0.78 to 1.58 GHz. The absence of “beam-squint” in the above frequency range shows that the antenna has a better than 50% instantaneous bandwidth.

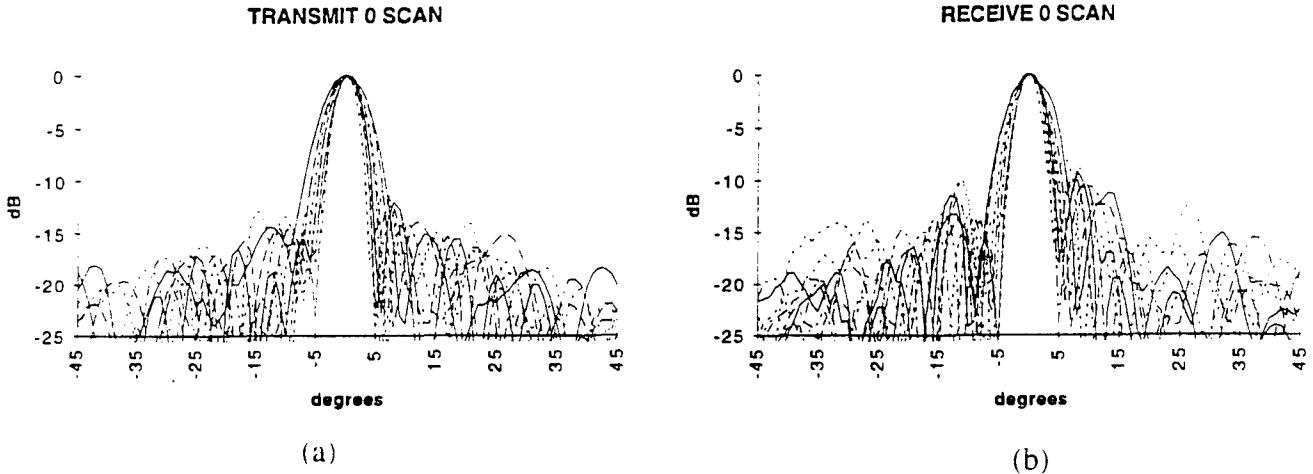


Figure 19. Broadside Patterns Obtained on (a) Transmit and (b) Receive.

5.2 FOLDED-CHIP VERSION OF THE SILICA-WAVEGUIDE MODULE

In the last quarter of the program, we experimented with further miniaturization of the silica-waveguide module. The basic length of the silica-waveguide module inserted into the L-band array was ~ 21.12 cm. This length was determined by the total length (15.32 cm) of the three silica-chips in the network - chip I (7.25 cm), 4×4 star-coupler chip (2 cm), chip II (6.07 cm) - and the length (~ 2.9 cm) of the two fiber-ribbon connectors located at the input and output ends of the network. If we fold the layout of the silica-waveguide chips inside the Al-housing, we can cut the length of the module by almost one-half. To accomplish that, we butt-coupled chip II to

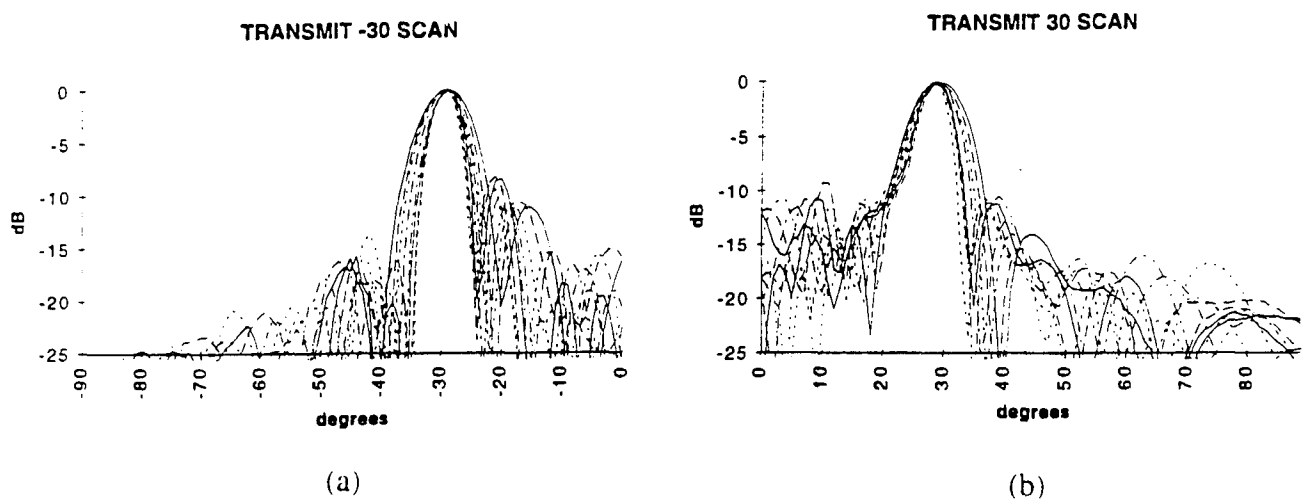


Figure 20. Transmit Patterns Obtained for (a) -30° and (b) $+30^\circ$ Scan.

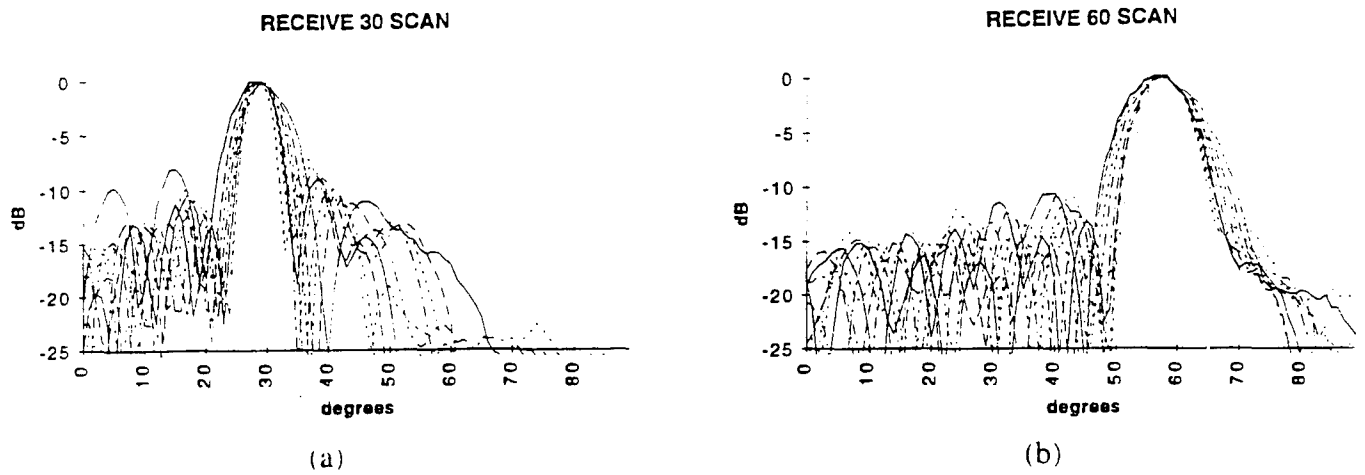


Figure 21. Receive Patterns Obtained for (a) $+30^\circ$ and (b) $+60^\circ$ Scan.

the star-coupler, and used a flexible fiber-ribbon to connect the star-coupler to chip I. Chip I and chip II were then attached, respectively, to the top and bottom plates of the module's Al-housing. Fig.22 shows a photograph of the module in which the waveguide-chips were "folded" in the manner described above. The silica-waveguide chips inside the module were fabricated with the use of the same designs and mask sets as before. As shown, the length of the module was only ~ 12.73 cm.

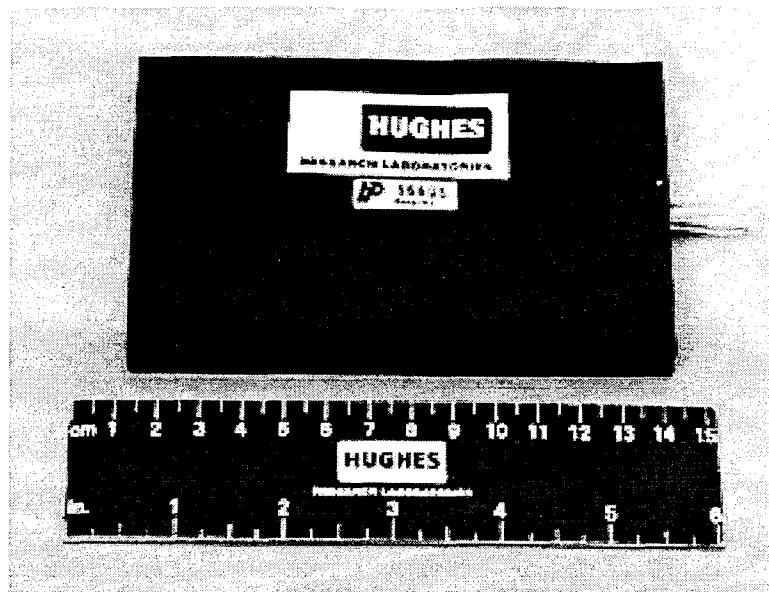


Figure 22. Photograph of the Waveguide-module with “Folded-chips”.

Ideally, the packaging procedure described above would only give rise to an additional ~ 0.5 dB of coupling loss. This additional coupling loss stems from the extra coupling-interface between chip I and the fiber-ribbon. In Table 4, we show the measured (optical) insertion losses of the various delay paths in the module of Figure 21. The designations of the rows and columns are the same as Table 3. Hence, the entries in the table represent a matrix of measured losses for delay-paths that connected the delay-lines of chip II (L_i , $i=5..8$) to those of chip I (L_j , $j=1..4$).

Table 4. Optical Insertion Loss of Folded-Chip Silica Waveguide Network.

L_i in dB (α in dB/cm)	L_5 (6 cm)	L_6 (11 cm)	L_7 (16 cm)	L_8 (21 cm)
L_1 (7.2 cm)	12.03	15.56	13.74	17.31
L_2 (27.2 cm)	13.16	17.30	15.18	17.99
L_3 (47.2 cm)	12.57	16.49	14.85	18.41
L_4 (67.2 cm)	13.81	17.93	15.08	18.33

Comparing Table 3 and Table 4, we see that the 16 delay-line combinations from both modules demonstrated very comparable optical insertion losses. Eight of the sixteen delay-line combinations from the folded-chip module actually exhibited lower insertion losses than what was given in Table 3. We attribute this to the fabrication of better waveguides, i.e. waveguides with lower propagation losses, in that particular run. For example, the waveguide combination of L₅ and L₄ (the longest delay-line of all) actually showed a propagation loss that was 3.23 dB lower in Table 4. Since L₅ was a straight waveguide, it is safe to assume that the loss reduction came from an improved fabrication run for L₄. Specifically, it showed that the loss per unit length (α) of L₄, a delay-line 67.2 cm long, was lowered by as much as 0.048 dB/cm. We note that a lowering of the insertion loss (by ~3.06 dB) was also observed for the delay-line combination that connected L₄ to L₇. The above results implied that delay-lines fabricated by the geometry designed for L₄ could actually exhibit a lower loss than what we had observed for the module (with the data tabulated in Table 3) inserted into the L-band array. This is very encouraging because our system-insertion experiment indicated that the longer delay-lines tended to bring down the overall level of the RF output from the photonic time-shifter.

On the other hand, we also observed a general increase in the insertion losses of the delay-line combinations that involved L₆ and L₈. By the same token, we can attribute the increase to (i) a poorer realization of the delay-line designs for L₆ and L₈, or (ii) a poorer coupling efficiency between them and the star-coupler. Since the waveguide designs for these rather short delay-lines (11 cm for L₆ and 21 cm for L₈) were relatively simple, we should be able to produce results at least as good as those tabulated in Table 3 if more fabrication runs were needed in the future.

Finally, we want to point out that these waveguide-based time-delay networks could be further miniaturized by adopting the Si-substrate as a hybrid integration platform. By mounting lasers and detectors on the Si-substrate where we fabricate the waveguide-delay-lines, we eliminate the fiber-ribbon connectors at each end. If the above is accomplished successfully, the waveguide-network - with hybridly integrated lasers and detectors - will be even more robust than what we demonstrated in this program.

5.3 CONCLUSION

In summary, we demonstrated a 4-bit optoelectronic-switched silica-waveguide time-delay network. Targeted for the central columns of a 96-element L-band conformal array, the programmable time-shifter provided 16 time-delays in steps of ~0.248 nsec. We accomplished the above objectives by integrating eight delay-lines on two silica-waveguide chips. In particular, the physical lengths of the delay-paths ranged from ~13.2 cm to ~88.2 cm on these chips. We measured propagation losses of less than 0.1 dB/cm for the waveguides in all sixteen

delay-paths. By using RF insertion phase measurements, we verified that the relative time-delays between the waveguides were within 15 psec of their designed values. In addition, the synthesized pulse responses of the packaged waveguide-network showed no broadening or distortion in all sixteen of its delay options. We also demonstrated a folded-chip version of the silica-waveguide network. Without incurring noticeable increases in the optical insertion loss, we were able to shorten the length of the waveguide-module (by almost a factor of two) by adopting a folded-chip package-design. Finally, we accomplished insertion of the silica-waveguide module into the 96-element conformal array. With the silica-waveguide module controlling one of its central columns, we demonstrated that the antenna possessed a better than 50% instantaneous bandwidth for scan angles as wide as $\pm 60^\circ$.

Section 6

REFERENCES

1. W. Ng, A. Walston, G. Tangonan, J.J. Lee, I. Newberg, and N. Bernstein, "The first demonstration of an optically steered microwave phased array antenna using true-time-delay," *IEEE J. Lightwave Technol.*, Vol. LT-9, pp. 1124-1131, 1991.
2. See, for example, Proc. SPIE Conf. for Optoelectronic Signal Processing for Phased-Array Antennas IV, Vol. 2155, 1994.
3. W. Ng, D. Yap, A. Narayanan, and A. Walston, "High-precision detector-switched monolithic GaAs time-delay network for the optical control of phased arrays," *IEEE Photon. Technol. Lett.*, Vol. 6, pp. 231-234. 1994.
4. J.J. Lee, S. Livingston, R. Loo, V. Jones, C. Foster, H.W. Yen, and G. Tangonan, "System design and performance of a wideband photonic array antenna," in Proc. SPIE Conf. for Optoelectronic Signal Processing for Phased-Array Antennas IV, Vol. 2155, pp. 287-295, 1994.
5. R.R. Hayes and D. Yap, "GaAs spiral optical waveguides for delay-line applications," *IEEE J. Lightwave Technol.*, Vol. LT-11, pp.523-528, 1993.

***MISSION
OF
ROME LABORATORY***

Mission. The mission of Rome Laboratory is to advance the science and technologies of command, control, communications and intelligence and to transition them into systems to meet customer needs. To achieve this, Rome Lab:

- a. Conducts vigorous research, development and test programs in all applicable technologies;
- b. Transitions technology to current and future systems to improve operational capability, readiness, and supportability;
- c. Provides a full range of technical support to Air Force Materiel Command product centers and other Air Force organizations;
- d. Promotes transfer of technology to the private sector;
- e. Maintains leading edge technological expertise in the areas of surveillance, communications, command and control, intelligence, reliability science, electro-magnetic technology, photonics, signal processing, and computational science.

The thrust areas of technical competence include: Surveillance, Communications, Command and Control, Intelligence, Signal Processing, Computer Science and Technology, Electromagnetic Technology, Photonics and Reliability Sciences.